PAPER

Check for updates

MnO$_2$/ZnCo$_2$O$_4$ with binder-free arrays on nickel foam loaded with graphene as a high performance electrode for advanced asymmetric supercapacitors

Wanjuan Cong,†[ab] Rui Miao,†[a] Bairui Tao [ID] *[a] and Fengjuan Miao [ID] *[a]

ZnCo$_2$O$_4$ nanosheets were successfully arrayed on a Ni foam surface with graphene using a hydrothermal method followed by annealing treatment; then MnO$_2$ nanoparticles were electrodeposited on the ZnCo$_2$O$_4$ nanosheets to obtain a synthesized composite binder-free electrode named MnO$_2$/ZnCo$_2$O$_4$/graphene/Ni foam (denoted as MnO$_2$/ZnCo$_2$O$_4$/G/NF). After testing the binder-free composite electrode of MnO$_2$/ZnCo$_2$O$_4$/G/NF *via* cyclic voltammetry, galvanostatic charge–discharge and electrochemical impedance spectroscopy testing, we found that it exhibited ultrahigh electrochemical properties, with a high specific areal capacitance of 3405.21 F g^{-1} under a current density of 2 A g^{-1}, and wonderful cycling stability, with 91.2% retention after 5000 cycles. Moreover, an asymmetric supercapacitor (ASC) based on MnO$_2$/ZnCo$_2$O$_4$/G/NF//G/NF was successfully designed. When tested, the as-designed ASC can achieve a maximum energy density of 46.85 W h kg^{-1} at a power density of 166.67 W kg^{-1}. Finally, the ASC we assembled can power a commercial red LED lamp successfully for more than 5 min, which proves its practicability. All these impressive performances indicate that the MnO$_2$/ZnCo$_2$O$_4$/graphene composite material is an outstanding electrode material for electrochemical capacitors.

1. Introduction

With societal development, and science and technology progress, the electronics industry urgently needs energy storage devices that are high-performance, lightweight and environmentally friendly to achieve sustainable and renewable energy.[1] For utilizing renewable sources, supercapacitors are one of the most promising candidates on account of their fast charging capabilities, high power densities and good cycling performances.[2] Although they have these excellent features, the relatively low energy densities of supercapacitors seriously limit their large-scale practical application.[3] Thus, it is necessary to improve the energy densities of supercapacitors to meet future energy demand. In recent years, it has been found that seeking the best electrode material is key to the development of supercapacitor research.[4] However, traditional electrode materials have been unable to meet the higher energy density requirements of supercapacitors. Therefore, developing new electrode materials with excellent properties is critical.

Recently, ternary ZnCo$_2$O$_4$ has attracted a great amount of research attention because its structure, a normal spinel structure with Zn^{2+} occupying the tetrahedral sites in the cubic spinel and Co^{3+} occupying the octahedral sites, renders ZnCo$_2$O$_4$ nanomaterials with high theoretical specific capacitances, excellent electrical conductivities, and rich active sites for redox reactions.[5–7] Meanwhile, it has the advantages of abundant availability, low cost and environmental friendliness.[8] However, it also presents problems, such as a low surface area and a large decrease in performance following long-term utilization. Adhering flexible materials to a conductive substrate to form a porous composite with channels conducive to the efficient diffusion of ions and the obtaining of high surface area, and the direct growth of hetero-structures on conductive substrates to make adequate use of the merits of different kinds of materials are viable ways to solve these issues. For instance, Gao *et al.* reported that the facile hydrothermal deposition of ZnCo$_2$O$_4$ nanoflakes on Ni foam with reduced graphene oxide could delivered a high capacitance of 860 F g^{-1} and high rate capabilities.[9] Li *et al.* successfully synthesized MnO$_2$/ZnCo$_2$O$_4$ nanosheet arrays with a specific capacitance of 286 F g^{-1} in a three-electrode system *via* a facile solvothermal method, and assembled supercapacitors exhibited a high energy density of 16.94 W h kg^{-1} at 750 W kg^{-1}.[10]

As is well known, graphene can serve as a skeleton for a variety of composite materials with enhanced supercapacitor performance

[a]College of Communications and Electronics Engineering, Qiqihar University, Heilongjiang 161006, China. E-mail: miaofengjuan@163.com; tbr_sir@163.com; Fax: +86-452-2738748; Tel: +86-452-2742787

[b]College of Computer and Information Engineering, Heihe University, Heilongjiang 164300, China

† Rui Miao and Wanjuan Cong are common first authors.
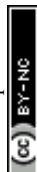
due to it being a conductive 2D flexible carbon material.[11] MnO_2 has advantages of having a high theoretical capacitance of up to 1370 F g^{-1}, being low cost and nontoxic, and having abundant resources, and it has been widely used in supercapacitors.[12] Therefore, considering the merits of these materials, combining $ZnCo_2O_4$ with graphene and MnO_2 would be propitious for further improving the energy densities of supercapacitors.

Based on the above discussion, in this study, we demonstrate a composite electrode comprising MnO_2 nanoparticles loaded on a porous $ZnCo_2O_4$ nanosheet material supported on graphene coated on a Ni foam substrate, which is shown in Fig. 1. Graphene was first dropped onto the Ni foam, and then the $ZnCo_2O_4$ material was grown on the graphene substrate *via* a simple hydrothermal strategy, followed by annealing treatment; finally, MnO_2 was deposited on the $ZnCo_2O_4$ substrate to form the $MnO_2/ZnCo_2O_4/graphene/Ni$ foam (denoted as $MnO_2/ZnCo_2O_4/G/NF$) electrode. The $MnO_2/ZnCo_2O_4/G/NF$ electrode can offer a maximum capacity of 3405.21 F g^{-1} at a current density of 2 A g^{-1} with good cycling stability, showing 91.2% retention after 5000 cycles at a consistent current density of 20 A g^{-1}. Furthermore, using $MnO_2/ZnCo_2O_4/G/NF$ as a positive electrode and G/NF as a negative electrode to assemble an asymmetric supercapacitor (ASC) results in excellent performance, with an energy density of 46.85 W h kg^{-1} at a power density of 166.67 W kg^{-1}.

2. Experimental details

2.1 Materials and reagents

Zinc nitrate hexahydrate ($Zn(NO_3)_2 \cdot 6H_2O$), cobalt nitrate hexahydrate ($Co(NO_3)_2 \cdot 6H_2O$) and urea ($CO(NH_2)_2$) were purchased from Shanghai Hansi Chemical Industry Co. Ltd. Absolute ethanol, manganese acetate ($Mn(CH_3COO)_2$), sodium sulphate (Na_2SO_4) and hydrochloric acid (HCl) were commercially available from Aladdin Chemical Co. All materials were analytical grade reagents, commercially available and used without any purification. Ni foam (thickness: 1.5 mm, pore density: 100 PPI, areal density: 380 g m^{-2}) was obtained from Changsha Lyrun New Materials Corporation. An oily slurry of graphene (5 wt%) was purchased from Suzhou Graphene Nanotechnology Co. Ltd. All solutions were prepared with deionized water throughout the experiments.

2.2 Preparation of the G/NF substrate

The Ni foam was cleaned in DI water, hydrochloric acid, DI water, absolute ethanol and DI water, respectively, for 5 min under ultrasonication. The Ni foam was then removed and put in a drying oven at 60 °C for 30 min. 0.5 g of graphene slurry was dispersed into 30 mL of absolute ethanol using mild water bath ultrasound technology. Then the solution was repeatedly dropped on the Ni foam. Finally, the Ni foam was dried at 60 °C for 1 h to acquire the graphene/Ni foam (G/NF) substrate.

2.3 Synthesis of $ZnCo_2O_4$ nanosheets on the G/NF substrate

To grow $ZnCo_2O_4$ nanosheets on the G/NF substrate, 0.44 g of $Zn(NO_3)_2 \cdot H_2O$, 0.86 g of $Co(NO_3)_2 \cdot H_2O$, and 0.424 g urea were dissolved in a mixed solution of 35 mL of H_2O and 5 mL of ethanol under magnetic stirring for 30 min to gain a homogeneous solution. The transparent solution was transferred into a 50 mL Teflon-lined stainless-steel autoclave. The prepared G/NF was dipped into the solution before sealing the autoclave. Subsequently, the autoclave was heated at 130 °C for 5 h to hydrothermally deposit the formed ZnCo precursor onto the G/NF substrate. After the hydrothermal process was finished, the
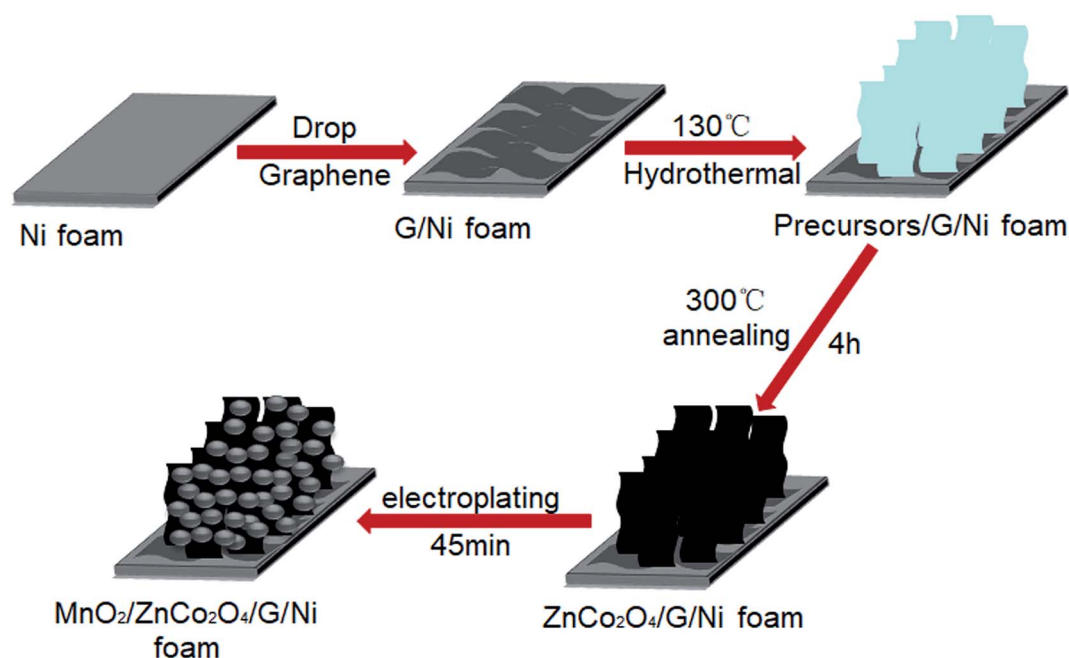

Fig. 1 A schematic illustration of the formation process of the $MnO_2/ZnCo_2O_4/G/NF$ composite electrode.

autoclave was removed from the electric oven and cooled to room temperature, and repeat rinses with deionized water were used to wash the sample to eliminate redundant activated material before drying at 60 °C for 3 h. Thereafter, the sample was annealed at 300 °C for 4 h in order to obtain thin layered nanosheets of $ZnCo_2O_4$ on the G/NF substrate. Under the same hydrothermal conditions but changing the annealing time to 2, 3 and 5 h, different electrodes were also prepared for comparison. In addition, a single $ZnCo_2O_4$ electrode without graphene was prepared to evaluate the effects of graphene on the capacitance performance.

2.4 Synthesis of MnO_2 nanoparticles on the $ZnCo_2O_4$/G/NF substrate

0.22 g of $Mn(CH_3COO)_2$ and 0.43 g of Na_2SO_4 were dissolved in 30 mL of DI water under ultrasonication with stirring for 10 min to obtain a homogeneous solution for electrodepositing MnO_2. Electrodeposition was performed at room temperature with Pt as the negative electrode and $ZnCo_2O_4$/G/NF as the positive electrode through adopting chronopotentiometry mode at a fixed current density of 1 mA cm^{-2} for 45 min to obtain the MnO_2/$ZnCo_2O_4$/G/NF electrode. In order to compare the performances of electrodes obtained after different plating times, the plating time was changed to 5, 15, 30 and 60 min to acquire different electrodes.

2.5 Apparatus and measurement procedures

The morphologies and microstructures of the electrode materials were analyzed *via* scanning electron microscopy (SEM, JSM-6360LA), field-emission transmission electron microscopy (TEM/HRTEM, JEM 2100F), and selected area electron diffraction (SAED) coupled with energy dispersive spectroscopy (EDS). The phases and crystal structures of the electrode materials were evaluated *via* X-ray powder diffraction (XRD, Rigaku, RINT2000, Japan). The chemical elements and their states in the electrode materials were examined *via* X-ray photoelectron spectroscopy (XPS, Axis Ultra DLD, Kratos, UK).

The electrochemical properties of the as-fabricated electrodes were measured using different electrochemical techniques, such as cyclic voltammetry (CV) and galvanostatic charge–discharge (GCD) tests on a CHI604E electrochemical workstation and electrochemical impedance spectroscopy (EIS) tests on a Zahner Ennium electrochemical workstation. The measurements were performed using a standard three-electrode configuration, with a prepared electrode, a platinum plate and a saturated calomel electrode (SCE) as the working electrode, counter electrode and reference electrode, respectively; 1 M Na_2SO_4 aqueous solution was used as the electrolyte.

3. Results and discussion

3.1 Morphology and structure of MnO_2/$ZnCO_2O_4$/G/NF electrode

The crystal structures of graphene, graphene coated with $ZnCo_2O_4$ nanosheets, and $ZnCo_2O_4$ nanosheets with MnO_2 nanoparticles loaded on graphene were confirmed *via* XRD measurements, as shown in Fig. 2. The XRD peaks at 16.6°, 26.5° and 36.449° were

indexed to the (002), (004) and (210) crystal planes of graphene. The XRD peaks at 31.3°, 36.9°, 59.7° and 65.2° were indexed to the (220), (311), (511) and (440) crystal planes of $ZnCo_2O_4$ (JCPDS No. 23-1390), respectively. In the XRD pattern of MnO_2/$ZnCo_2O_4$/G/NF, $ZnCo_2O_4$ and graphene peaks could be observed, while the presence of MnO_2 was not confirmed. The existence of MnO_2 can be verified from SEM studies, as shown in Fig. 3d and e, and EDS data, as shown in Fig. 4a. The two sharp peaks marked with "♣" corresponded to the Ni foam substrate.[13]

The structure of graphene on a Ni foam substrate has been presented in our previous paper.[14] Fig. 3a shows a low magnification SEM image of the sample grown on the G/NF substrate, indicating the formation of $ZnCo_2O_4$ nanosheets. In Fig. 3b, further observations show that the $ZnCo_2O_4$ nanosheets are densely packed and highly uniform, like a forest grown on the G/NF substrate. The nanosheets are interlinked with each other, showing a more stable structure, which enhances the surface area of the material significantly. In addition, the holes between nanosheets can be used as operating transmission channels for the electrolyte during the charging/discharging process. In Fig. 3c, a high magnification SEM image of the sample grown on the G/NF substrate is shown, revealing that the $ZnCo_2O_4$ nanosheets are connected to each other with adequate space between each individual nanosheet, and the nanosheets possess smooth surfaces with an average length of 1.08 μm. This structure provides large spaces for the growth of MnO_2 nanoparticles and is extremely beneficial for the formation of heterostructures. Compared with Fig. 3c, d and e reveal different magnification SEM images of the composite materials, indicating that the MnO_2 nanoparticles are uniformly deposited on the $ZnCo_2O_4$ nanosheets. In Fig. 3e, it can be seen more clearly that the core $ZnCo_2O_4$ nanosheets are wrapped in thousands of small MnO_2 nanoparticles, which make the composites more intense and thicker. The uniformly deposited MnO_2 on the $ZnCo_2O_4$ nanosheets can promote ion/electron transport between the electrode and electrolyte, which is essential for improving the electrochemical performance. More detailed information about the morphological characteristics of the composite materials was obtained *via* TEM, HR-TEM and SAED, as shown in Fig. 3f–i. Fig. 3f and g shows TEM images at different magnifications of the MnO_2 nanoparticles
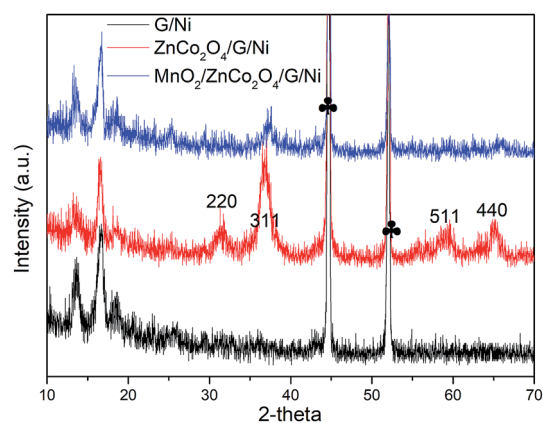

Fig. 2 XRD patterns of $ZnCo_2O_4$, graphene coated with $ZnCo_2O_4$, and $ZnCo_2O_4$ with MnO_2 loaded on graphene.
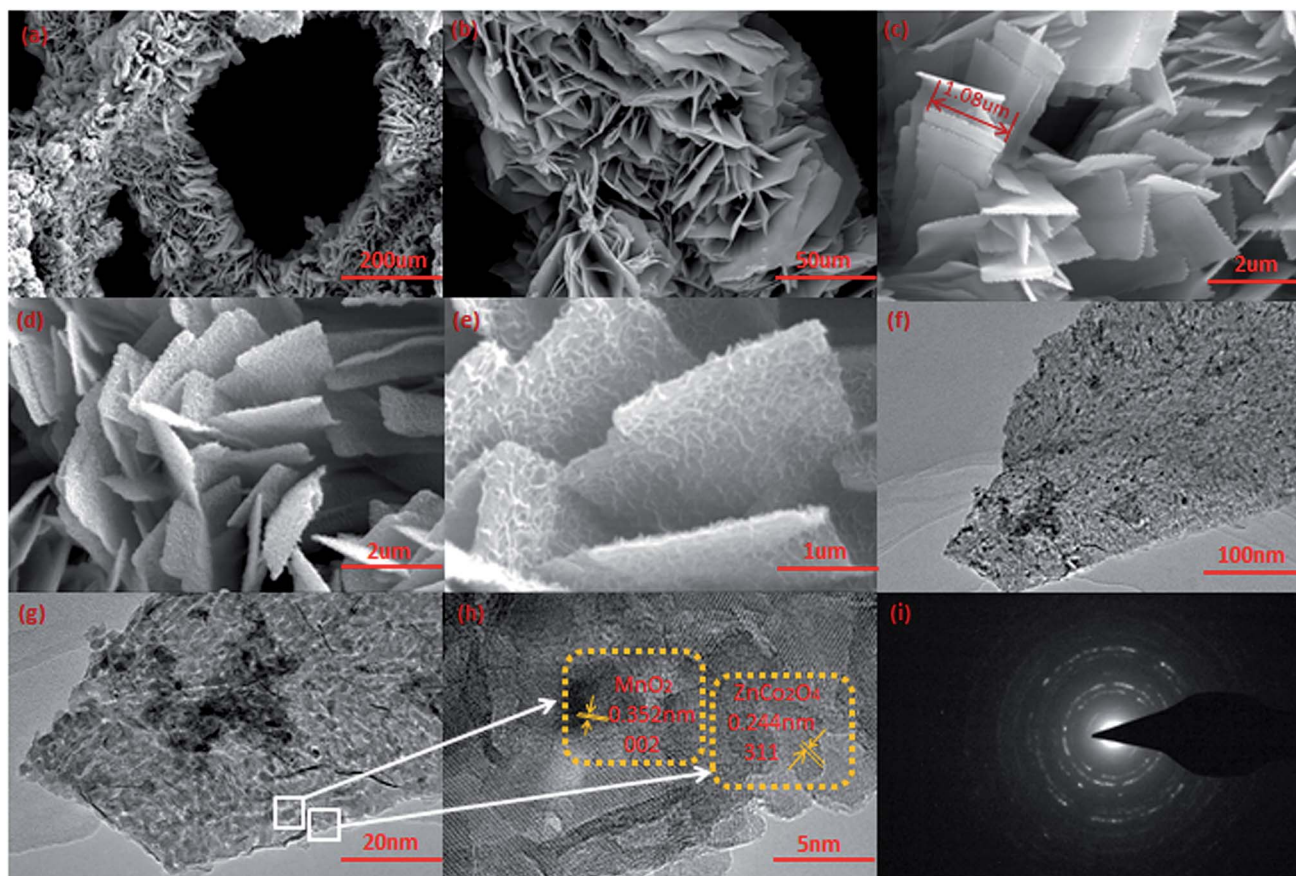
Fig. 3 (a)–(c) SEM images of $ZnCo_2O_4$ nanosheets; (d) and (e) SEM images of $ZnCo_2O_4$ nanosheets with MnO_2 nanoparticles; (f and g) TEM images at different magnifications of $ZnCo_2O_4$ nanosheets with MnO_2 nanoparticles; (h) a HR-TEM image of $ZnCo_2O_4$ nanosheets with MnO_2 nanoparticles; and (i) a SAED image of $ZnCo_2O_4$ nanosheets with MnO_2 nanoparticles.

coated on one of the $ZnCo_2O_4$ nanoflakes; it can be seen clearly that the MnO_2 nanoparticles have grown on the surface of $ZnCo_2O_4$. Therefore, this heterostructure significantly increases the effective number of electrochemical active sites on the electrode. Fig. 3h displays a HR-TEM image; this shows a lattice fringe of 0.352 nm, which is consistent with the MnO_2 (002) plane, and one of 0.244 nm, which matches well with the spacing of the (311) plane of $ZnCo_2O_4$. The selected area electron diffraction (SAED) pattern shows a clear polycrystalline structure, as shown in Fig. 3i. In addition, EDS mapping analysis of the elemental composition of $MnO_2/ZnCo_2O_4/G/NF$ affirms that $ZnCO_2O_4$, MnO_2 and a graphene composite are attached to the nickel foam substrate, as shown in Fig. 4a.

The formation of the G/NF-substrate-supported $MnO_2/ZnCo_2O_4$ composite was further analyzed *via* XPS. Fig. 4b shows the XPS survey spectrum, indicating the presence of five distinct peaks, which are Zn 2p, Co 2p, Mn 2p, O 1s, and C1s, confirming the presence of Zn, Co, Mn, O and C. The core level spectrum of the Zn 2p region is revealed in Fig. 4c; the two strong peaks with binding energies of 1020.98 and 1043.78 eV correspond to Zn 2p3/2 and Zn 2p1/2, respectively, thus indicating the Zn^{2+} oxidation state of $ZnCo_2O_4$ in $MnO_2/ZnCo_2O_4/G/NF$.[15] The Co 2p spectrum is shown in Fig. 4d; two major peaks at 779.98 and 794.88 eV are visible, which are assigned to the spin-orbits of Co 2p3/2 and Co 2p1/2, with a splitting value above 14.9 eV. Both

peaks also can be separated into two peaks, suggesting the presence of Co^{2+} and Co^{3+} in the form of cobaltate.[16] Fig. 4e shows the presence of Mn ions in the oxide form of MnO_2 with binding energies of 642.18 eV and 653.98 eV, relating to Mn 2p3/2 and Mn 2p1/2, respectively. The separation of the peak energy is 11.7 eV, which agrees well with previously reported data by Montree Sawangphruk *et al.*, strongly suggesting that the oxidation state of Mn is +4.[17] The detailed O 1s spectrum is displayed in Fig. 4f; one peak at 529.68 eV points to the formation of oxides with Zn–Co and Mn. The other peak at 531.38 eV can be thought of as resulting from a multiplicity of physically and chemically bonded oxygen on and within the surface.[18] The SEM, TEM, XRD and XPS results show that the $MnO_2/ZnCo_2O_4/G/NF$ composite material electrode has been successfully fabricated.

3.2 Characterization of the $MnO_2/ZnCo_2O_4/G/NF$ electrode

In order to establish the best annealing time for the $ZnCo_2O_4$ electrode material and the optimal length of time for the electrodeposition of MnO_2 on the $ZnCo_2O_4$ electrode, the electrochemical properties of a number of samples were measured in a typical three electrode system, using 1 M Na_2SO_4 as the electrolyte, *via* CV, GCD and EIS measurements. Fig. 5a shows the
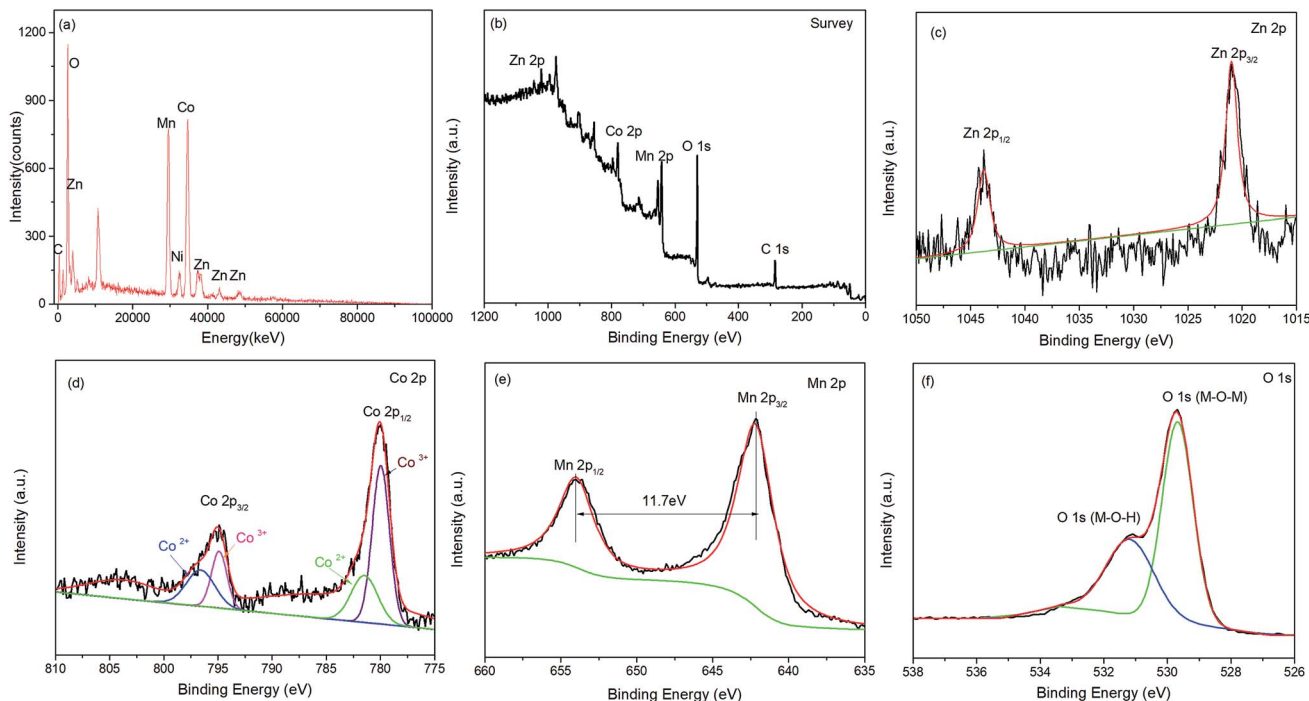
Fig. 4 (a) The EDS spectrum of the $MnO_2/ZnCo_2O_4/G/NF$ electrode; (b) the XPS survey spectrum of the $MnO_2/ZnCo_2O_4/G$ composite; (c) the core-level spectrum of Zn 2p; (d) the core-level spectrum of Co 2p; (e) the core-level spectrum of Mn 2p; and (f) the core-level spectrum of O 1s.

CV curves from different $ZnCo_2O_4$ annealing times on the G/NF substrate (the annealing time is 4 h for the electrodes with pure $ZnCo_2O_4$ on the Ni substrate and graphene on the Ni substrate), which were obtained in the potential window of 0–0.6 V at a scan rate of 50 mV s^{-1}. It can be seen clearly that the CV of G/NF is a straight line in the picture and the CV area of $ZnCo_2O_4$/G/NF is larger than the CV area of $ZnCo_2O_4$/NF, indicating that graphene provides more attachment sites for $ZnCo_2O_4$. Among the samples, the $ZnCo_2O_4$/G/NF electrode annealed for 4 h is better than the other electrodes. On this basis, different MnO_2 electrodeposition times were studied for loading on the $ZnCo_2O_4$/G/NF electrode and the CV curves are shown in Fig. 5b. With an increase in the MnO_2 deposition time, the capacitive current and CV area increase gradually, indicating that MnO_2 indeed increased the capacitance of the $ZnCo_2O_4$/G/NF

electrode. There was a decrease when the deposition time was more than 45 min, which might be due to thicker layers of MnO_2 preventing the transportation of electrolyte ions to some extent. $MnO_2/ZnCo_2O_4$/G/NF shows better performance than the other electrodes. Fig. 5c shows CV curves from $MnO_2/ZnCo_2O_4$/G/NF at different scan rates ranging from 10 to 100 mV s^{-1}. With an increase in the scan rate, the CV curve becomes steeper and no redox peaks are observed, which may have been because of the overlapping of peaks resulting from multiple redox transitions, lattice defects creating active sites with slightly varying redox potentials, and $ZnCo_2O_4$ and MnO_2 surface reactions on the electrodes;[19] however, the electrodes still show pseudo-capacitive symmetry behavior.

To further prove the electrochemical behavior of the $MnO_2/ZnCo_2O_4$/G/NF electrode, Fig. 6 depicts GCD curves from all

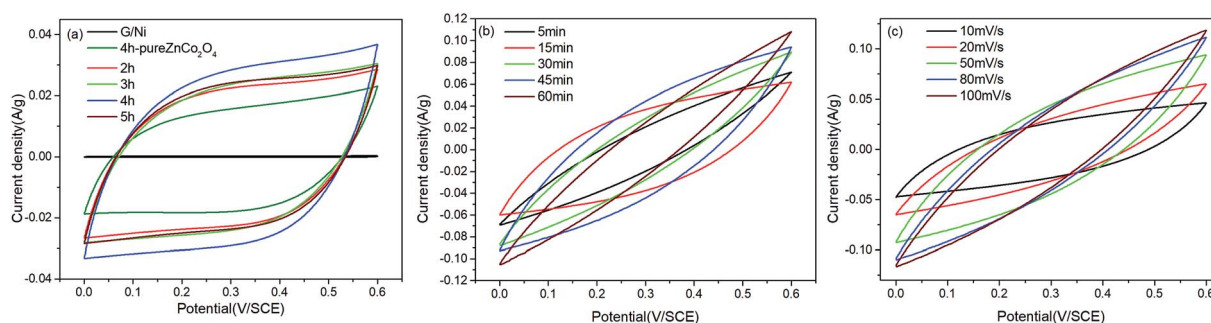**Fig. 5** (a) CV curves recorded at 20 mV s^{-1} of $ZnCo_2O_4$/G/NF composite electrodes synthesized with different annealing times and pure $ZnCo_2O_4$; (b) CV curves recorded at 20 mV s^{-1} of $MnO_2/ZnCo_2O_4$/G/NF composite electrodes synthesized with different electrodeposition times; and (c) CV curves of $MnO_2/ZnCo_2O_4$/G/NF recorded at different scan rates.

electrodes in a potential window ranging from 0 to 0.5 V. The GCD curves from the pure $ZnCo_2O_4$ electrode and electrodes with different $ZnCo_2O_4$ annealing times on the G/NF substrate at a current density of 2 A g^{-1} are displayed in Fig. 6a. Evidently, the GCD curves are almost symmetrical in morphology, indicating the presence of $ZnCo_2O_4$ thin films with good pseudocapacitive properties. Meanwhile, a $ZnCo_2O_4$ annealing time of 4 h on the G/NF substrate leads to the longest charge–discharge time, which means that it has better performance than the other electrodes. Then GCD curves from different MnO_2 electrodeposition times on the $ZnCo_2O_4$/G/NF electrodes are shown in Fig. 6b. The GCD curves still remain basically symmetrical and the corresponding discharge times are longer than those of the $ZnCo_2O_4$/G/NF electrodes at the same current density. Fig. 6c shows the GCD curves from MnO_2/$ZnCo_2O_4$/G/NF electrodes at different current densities from 2 to 20 A g^{-1}. Specific capacitance values were calculated according to the equation:

$$C = I\Delta t/m\Delta V \tag{1}$$

where C is the specific capacitance, I is the discharge current, Δt is the discharge time, m is the mass of electrode material, and ΔV is the potential window of the discharge process. In experiments, the quantities of graphene, $ZnCo_2O_4$ and MnO_2 on one piece of Ni foam were about 0.68 mg, 2.11 mg, and 1.05 mg, respectively. So, the mass loading on the electrode was about 3.84 mg. Through calculations, the MnO_2/$ZnCo_2O_4$/G/NF electrode exhibits a rather high specific capacitance of 3405.21 F g^{-1} at a current density of 2 A g^{-1} and a specific capacitance of

2208.3 F g^{-1} even at a high current density of 20 A g^{-1}. Fig. 6d displays the specific capacitance curves for electrodes made with different MnO_2 electrodeposition times on $ZnCo_2O_4$/G/NF at different current densities. The results are consistent with CV measurements. This electrochemical behavior of the enhanced MnO_2/$ZnCo_2O_4$/G/NF electrode can be attributed to its three-dimensional nanostructures and intrinsically good electro-conductivity.[20] The cycling stability of the MnO_2/$ZnCo_2O_4$/G/NF electrode is checked through GCD tests at a constant current density of 20 A g^{-1} for 5000 cycles, as depicted in Fig. 6e. In the first 900 cycles, the specific capacitance decreases first and then increases to 1441.67 F g^{-1}, which can be attributed to a wetting process involving electrolyte penetration into the material. After 1400 cycles, the specific capacitance decreases slightly to 1375 F g^{-1}, then tends to stay stable, keeping 91.2% of the initial capacitance. The insets (a) and (b) in Fig. 6e show a comparison of the last three cycles with the first three cycles, and the morphological changes in the MnO_2/$ZnCo_2O_4$/G/NF electrode after 5000 cycles at a current density of 20 A g^{-1}, respectively. From inset (a) of Fig. 6e, it can be seen that the shapes of the last three cycles are almost the same as the first three cycles, which proves the outstanding cycling behavior and that the electrode materials have good stability. From inset (b) of Fig. 6e, the $ZnCo_2O_4$ sheets with MnO_2 nanoparticles have become thinner due to ion transport to the inner and outer surfaces of the MnO_2/$ZnCo_2O_4$/G/NF electrode during the process of repeating charge–discharge. However, the electrode still maintains the $ZnCo_2O_4$ framework without collapse. The results indicate that
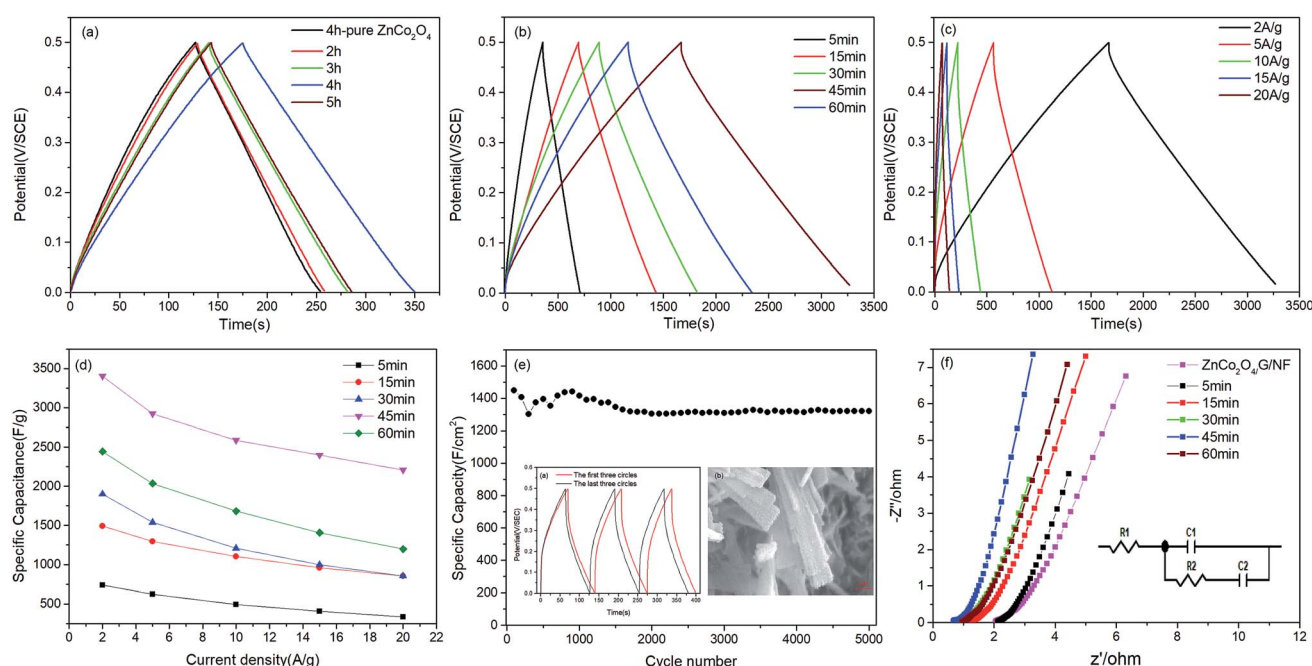

Fig. 6 (a) GCD curves recorded at 2 A g^{-1} of $ZnCo_2O_4$/G/NF composite electrodes synthesized with different annealing times and pure $ZnCo_2O_4$; (b) GCD curves recorded at 2 A g^{-1} of MnO_2/$ZnCo_2O_4$/G/NF composite electrodes synthesized with different electrodeposition times; (c) GCD curves of MnO_2/$ZnCo_2O_4$/G/NF electrodes recorded at different current densities; (d) the specific capacitances of $ZnCo_2O_4$/G/NF electrodes with different MnO_2 electrodeposition times at various current densities; (e) the cycling stability of the MnO_2/$ZnCo_2O_4$/G/NF electrode at 20 A g^{-1} (inset (a) is a comparison of the shapes of the first three cycles and last three cycles; inset (b) is a SEM image taken after 5000 cycles); and (f) Nyquist plots of $ZnCo_2O_4$/G/NF and $ZnCo_2O_4$/G/NF electrodes with different MnO_2 electrodeposition times.

the electrode materials have good corrosion resistance and further prove that the electrode materials have good stability.

As well as CV and GCD measurements, the impedance spectra of ZnCo$_2$O$_4$/G/NF electrodes with different MnO$_2$ electrodeposition times from 5 to 60 min with an annealing time of 4 h were obtained in the frequency range from 100 kHz to 0.01 Hz with a perturbation of 5 mV. The corresponding Nyquist plots in Fig. 6f can be fitted with an equivalent circuit (inset of Fig. 6f). It can be seen from the figure that when the electrodeposition time is less than 45 min, in the low frequency region, the slope is far higher than 45°; as the electrodeposition time increases, the lines become more vertical, which means a higher transmission efficiency of electrolyte. In the high frequency region, as the electrodeposition time increases, the intercepts with the real axis decrease gradually, which means the equivalent series resistance becomes lower.[21,22] When the electrodeposition time is 45 min, the equivalent resistance of the electrode is 0.66 Ω lower than those of the other electrodes. When the electrodeposition time exceeds 45 min, it can be seen from the low-frequency and high-frequency regions that excess MnO$_2$ aggregation prevents the transfer of ions/electrons, which reduces the electrochemical performance of the electrode.

3.3 Preparation of an asymmetric supercapacitor

To further test the potential of the MnO$_2$/ZnCo$_2$O$_4$/G/NF electrode for actual applications, a MnO$_2$/ZnCo$_2$O$_4$/G/NF electrode as the positive electrode, a G/NF electrode as the negative electrode and a piece of cellulose paper as the separator were used to fabricate an asymmetric supercapacitor. Fig. 7 shows the electrochemical performance testing of the as prepared ASC in 1 M Na$_2$SO$_4$ electrolyte. Fig. 7a displays the CV curves of the

as prepared ASC device recorded at a scan rate of 20 mV s^{-1} in different voltage windows. Obviously, the redox current increases with an increase in the voltage window, showing more significant pseudo-capacitance characteristics in a larger voltage range. When the voltage window reached 1.8 V, the CV curves became distorted because of some side reactions. Meanwhile, the GCD curves of the ASC device in different voltage windows at a current density of 1 A g^{-1} are shown in Fig. 7b, which indicate that the ideal voltage window of the ASC is 1.6 V. Hence, 1.6 V is selected as the maximized voltage window of the ASC to further evaluate the overall electrochemical performance. CV curves from the ASC device at different scan rates from 10 to 100 mV s^{-1} are shown in Fig. 7c. The CV curves still retain a fairly symmetrical shape upon increasing the scan rate, which indicates the good rate capabilities and good reversibility of the ASC. As presented in Fig. 7d, GCD curves at different current densities are almost symmetric, affirming that the as prepared ASC device has ASC-type capacitor behavior, consistent with the CV results. It was discovered in Fig. 7e that the specific capacitance of the ASC device is 131.77 F g^{-1} at 0.5 A g^{-1} and it even remains at 48.18 F g^{-1} upon increasing the current density to 5 A g^{-1}, which displays the fine rate capabilities. Moreover, the cycling stability is an important indicator for estimating the properties of an ASC. According to the data, Fig. 7f implies that the specific capacitance decreases slowly with increasing cycle number; after 800 cycles, it tends to be stable, and even after 5000 cycles, 90.5% of the initial capacitance is retained. Additionally, the energy density and power density are the key indexes of an ASC, which can be calculated based on the GCD data and these equations:
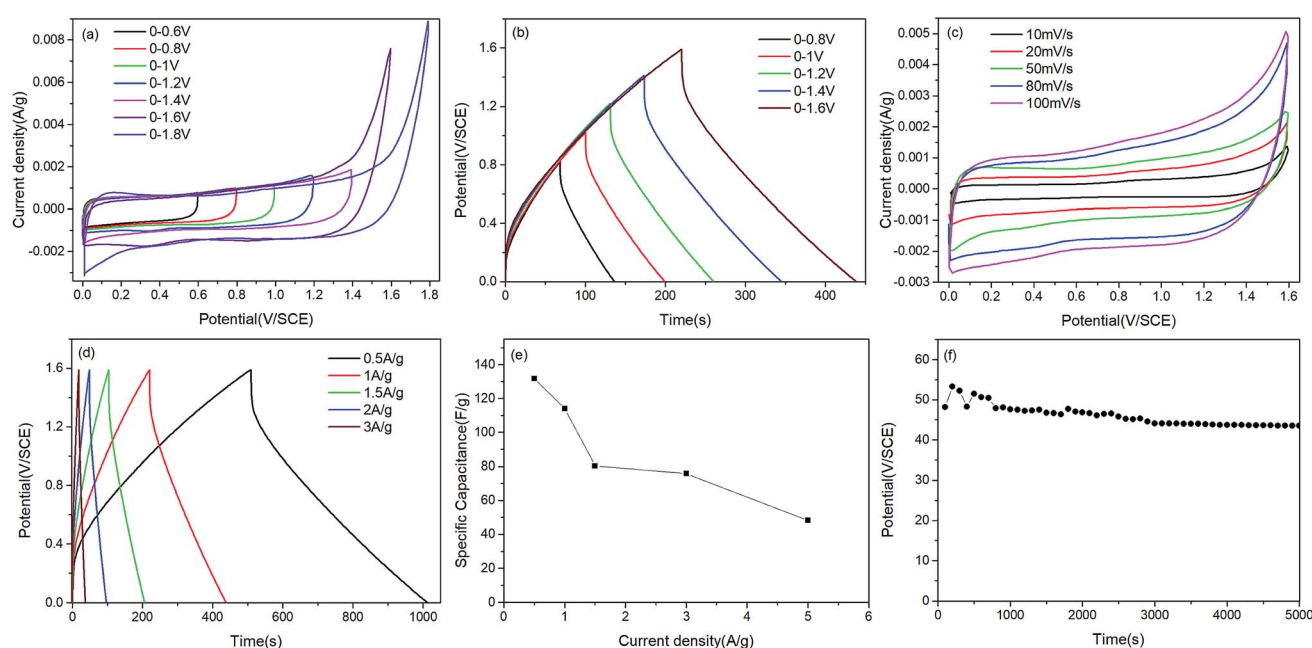

Fig. 7 (a) CV curves of ASC devices within different voltage windows at a scan rate of 20 mV s; (b) GCD curves of ASC devices within different potential windows at a current density of 3 A g; (c) CV curves at different scan rates from the ASC device; (d) GCD curves at different current densities from the ASC device; (e) the specific capacities of the ASC device at different current densities; and (f) the cycling stability of the ASC device.
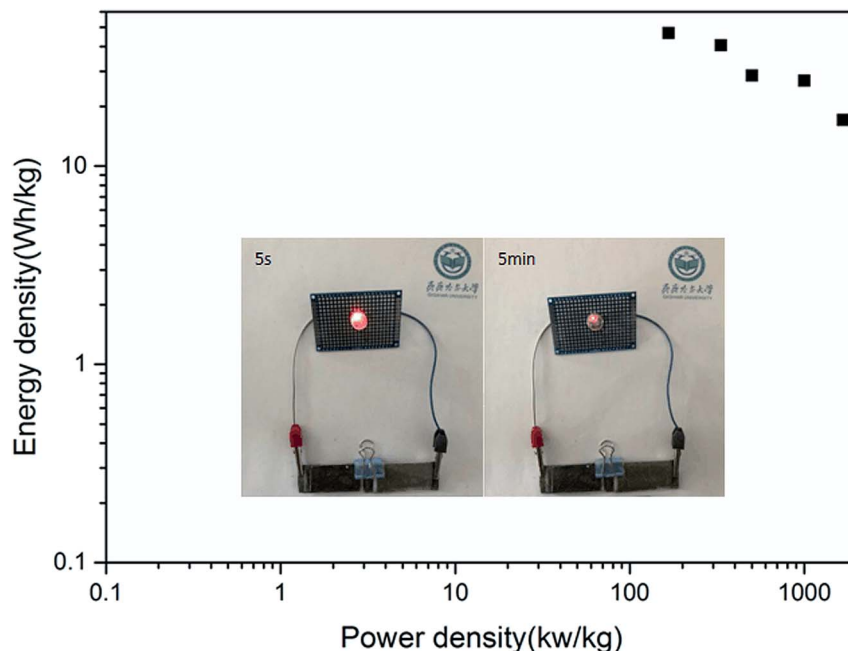
Fig. 8 A Ragone plot of the ASC device (the inset shows an image of a commercial red LED at different times after lighting).

Table 1 A comparison of various $ZnCo_2O_4$ nanostructures as electrode materials for SCs

Electroactive material	Maximum SC (F g^{-1} (mF cm^{-2}))	Current density (A g^{-1} (mA cm^{-2}))	Energy density (W h kg^{-1})	Power density (W kg^{-1})	Cycling stability (%)	Reference
$ZnCo_2O_4$	183.54	1.72	42.83	425	92.5 (10 000 cycles)	6
$ZnCo_2O_4/MnO_2$	161	2.5	37.8	648	91 (5000 cycles)	8
$ZnCo_2O_4/MnO_2$	54.2	1	16.94	7500	98.5 (1500 cycles)	10
$ZnCo_2O_4/MnCo_2O_4$	60	1	19.5	750	98.5 (2000 cycles)	19
$ZnCo_2O_4/rGO$	101	0.5	31.25	375	97.3 (2000 cycles)	21
$MnO_2/ZnCo_2O_4/graphene$	131.78	0.5	46.85	1666.67	90.5 (5000 cycles)	Our work

$$E = \frac{1}{2} C \Delta V^2 \qquad (2)$$

$$P = \frac{E}{t} \qquad (3)$$

The resulting values are drawn up in the form of a Ragone plot, as presented in Fig. 8. The ASC device that we prepared showed an energy density of 46.85 W h kg^{-1} at a power density of 166.67 W kg^{-1}, and this still remained at 17.13 W h kg^{-1} at a maximum power density of 1666.67 W kg^{-1}. These values are better than others reported, as shown in Table 1. In the end, the ASC we assembled can power a commercial red LED lamp successfully for more than 5 minutes, which indicates its practicability, as shown in the inset of Fig. 8.

4. Conclusions

In summary, mesoporous $ZnCo_2O_4$ nanosheets and uniformly distributed MnO_2 nanoparticle composites were successfully synthesized on a G/NF substrate *via* a one-step hydrothermal process followed by annealing and a one-step electrodeposition process. In addition, we found that, under the same hydrothermal conditions, the composite electrode with an annealing time of 4 h and a MnO_2 electroplating time of 45 min has better electrochemical properties. The synergistic effects of the MnO_2 nanoparticles, $ZnCO_2O_4$ nanosheets and graphene arrays on the Ni foam substrate enable the binder-free electrode to exhibit a specific capacitance of 3405.21 F g^{-1} at a current density of 2 A g^{-1} and it maintains capacitance retention of about 64.85% at 20 A g^{-1}. Furthermore, the capacitance remained at 91.2% at a current density of 20 A g^{-1} after 5000 cycles, and the electrode exhibits outstanding stability. An ASC was made with $MnO_2/ZnCO_2O_4/G/NF$ as the anode and G/NF as the cathode. The device delivers a high specific capacitance of 131.78 F g^{-1} at 0.5 A g^{-1} and cycling stability, with 90.5% retention after 5000 cycles, working in a large potential range of 0–1.6 V. It also exhibits a high energy density of 46.85 W h kg^{-1} and a maximum power density of 1666.67 W kg^{-1}. These excellent results confirm that combining porous $ZnCo_2O_4$ nanosheets with MnO_2 nanoparticles in a composite material is a promising approach in the field of energy storage.

Conflicts of interest

There are no conflicts to declare.

Acknowledgements

References

1 Y. Shang, et al., Synthesis of hollow $ZnCo_2O_4$ microspheres with enhanced electrochemical performance for asymmetric supercapacitor, Electrochim. Acta, 2018, 286, 103–113.

2 S. R. Suryawanshi, et al., Pt-nanoparticle functionalized carbon nano-onions for ultra-high energy supercapacitors and enhanced field emission behaviour, RSC Adv., 2015, 5, 80990–80997.

3 L. Lin, et al., 3D $ZnCo_2O_4$ nanowires@MnO_2 nanosheets core–shell structures grown on carbon cloth for excellent supercapacitor electrodes, Ceram. Int., 2016, 42(16), 19343–19348.

4 S. Vijayakumar, et al., Porous thin layered nanosheets assembled $ZnCo_2O_4$ grown on Ni-foam as an efficient electrode material for hybrid supercapacitor applications, Int. J. Hydrogen Energy, 2017, 42(5), 3122–3129.

5 L. Xu, et al., Morphology controlled preparation of $ZnCo_2O_4$ nanostructures for asymmetric supercapacitor with ultrahigh energy density, Energy, 2017, 123, 296–304.

6 J. Zhu, D. Song, T. Pu, et al., Two-dimensional Porous $ZnCo_2O_4$, Thin Sheets Assembled by 3D Nanoflake Array with Enhanced Performance for Aqueous Asymmetric Supercapacitor, Chem. Eng. J., 2017, 336, 679–689.

7 V. Venkatachalam, et al., Double hydroxide mediated synthesis of nanostructured $ZnCo_2O_4$ as high performance electrode material for supercapacitor applications, Chem. Eng. J., 2017, 321, 474–483.

8 M. Wenqin, N. Honghong, G. Zhengxiang, et al., Superior performance asymmetric supercapacitors based on $ZnCo_2O_4$@MnO_2 core–shell electrode, J. Mater. Chem. A, 2015, 3, 5442–5448.

9 Z. Gao, et al., $ZnCo_2O_4$-reduced graphene oxide composite with balanced capacitive performance in asymmetric supercapacitors, Appl. Surf. Sci., 2018, 442, 138–147.

10 L. Huanhuan, W. Lei, G. Yuming, et al., Facile solvothermal synthesis of ZnCo2O4/MnO2 nanosheets composite with enhanced electrochemical properties as supercapacitor electrodes, Appl. Phys. A: Mater. Sci. Process., 2018, 124(7), 485–495.

11 J. Qi, et al., Facile synthesis of mesoporous $ZnCo_2O_4$ nanosheet arrays grown on rGO as binder-free electrode for high-performance asymmetric supercapacitor, J. Mater. Sci., 2018, 53(23), 16074–16085.

12 X. Jia, X. Wu and B. Liu, Formation of $ZnCo_2O_4$@MnO_2 core–shell electrode materials for hybrid supercapacitor, Dalton Trans., 2018, 47(43), 15506–15511.

13 S. Sahoo and J. Shim, Facile Synthesis of Three-Dimensional Ternary $ZnCo_2$ O_4/Reduced Graphene Oxide/NiO Composite Film on Nickel Foam for Next Generation Supercapacitor Electrodes, ACS Sustainable Chem. Eng., 2016, 5(1), 241–251.

14 F. Miao, et al., Graphene/nano-ZnO hybrid materials modify Ni-foam for high-performance electrochemical glucose sensors, Ionics, 2018, 24(12), 4005–4014.

15 F. Qu, et al., Self-sacrificing templated formation of Co_3O_4/$ZnCo_2O_4$ composite hollow nanostructures for highly sensitive detecting acetone vapor, Sens. Actuators, B, 2018, 273, 1202–1210.

16 S. Sahoo, et al., Electrodeposited Nickel Cobalt Manganese based mixed sulfide nanosheets for high performance supercapacitor application, Microporous Mesoporous Mater., 2017, 244, 101–108.

17 R. Ponnusamy, et al., Improved Nonenzymatic Glucose Sensing Properties of Pd/MnO_2 Nanosheets: Synthesis by Facile Microwave-Assisted Route and Theoretical Insight from Quantum Simulations, J. Phys. Chem. B, 2018, 122(31), 7636–7646.

18 V. S. Kumbhar, et al., Hierarchical coating of MnO_2, nanosheets on $ZnCo_2O_4$, nanoflakes for enhanced electrochemical performance of asymmetric supercapacitors, Electrochim. Acta, 2018, 271, 284–296.

19 L. Wang, et al., $ZnCo_2O_4$@$MnCo_2O_4$ heterojunction structured nanosheets for high-performance supercapacitor, J. Mater. Sci.: Mater. Electron., 2018, 29(7), 5782–5790.

20 X. Li, et al., Annealing temperature dependent $ZnCo_2O_4$ nanosheet arrays supported on Ni foam for high-performance asymmetric supercapacitor, J. Alloys Compd., 2019, 773, 367–375.

21 Q. Jiqiu, M. Jingwen, Z. Anbang, et al., Facile synthesis of mesoporous $ZnCo_2O_4$ nanosheet arrays grown on rGO as binder-free electrode for high-performance asymmetric supercapacitor, J. Mater. Sci., 2018, 53, 16074–16085.

22 R. Samal, et al., Facile Production of Mesoporous WO_3-rGO Hybrids for High-Performance Supercapacitor Electrodes: An Experimental and Computational Study, ACS Sustainable Chem. Eng., 2019, 7, 2350–2359.